Nano Research
2020, 13(1): 127–132

ISSN 1998-0124 CN 11-5974/O4
https://doi.org/10.1007/s12274-019-2583-5

Research Article

Ultrahigh sensitive near-infrared photodetectors based on $MoTe_2$/germanium heterostructure

Wenjie Chen[1,2], Renrong Liang[1,2] (✉), Shuqin Zhang[1,2], Yu Liu[1,2], Weijun Cheng[1,2], Chuanchuan Sun[3], and Jun Xu[1,2] (✉)

[1] *Institute of Microelectronics, Tsinghua University, Beijing 100084, China*
[2] *Beijing National Research Center for Information Science and Technology (BNRist), Tsinghua University, Beijing 100084, China*
[3] *Beijing Institute of Control Engineering, Beijing 100084, China*

Received: 11 September 2019 / **Revised:** 13 November 2019 / **Accepted:** 27 November 2019

ABSTRACT

The efficient near-infrared light detection of the $MoTe_2$/germanium (Ge) heterojunction has been demonstrated. The fabricated $MoTe_2$/Ge van der Waals heterojunction shows excellent photoresponse performances under the illumination of a 915 nm laser. The photoresponsivity and specific detectivity can reach to 12,460 A/W and 3.3×10^{12} Jones, respectively. And the photoresponse time is 5 ms. However, the $MoTe_2$/Ge heterojunction suffers from a large reverse current at dark due to the low barrier between $MoTe_2$ and Ge. Therefore, to reduce the reverse current, an ultrathin GeO_2 layer deposited by ozone oxidation has been introduced to the $MoTe_2$/Ge heterojunction. The reverse current of the $MoTe_2/GeO_2$/Ge heterojunction at dark was suppressed from 0.44 $\mu A/\mu m^2$ to 0.03 $nA/\mu m^2$, being reduced by more than four orders of magnitude. The $MoTe_2$/Ge heterojunction with the GeO_2 layer also exhibits good photoresponse performances, with a high responsivity of 15.6 A/W, short response time of 5 ms, and good specific detectivity of 4.86×10^{11} Jones. These properties suggest that $MoTe_2$/Ge heterostructure is one of the promising structures for the development of high performance near-infrared photodetectors.

KEYWORDS

heterojunction, photodetector, $MoTe_2$, Ge, near-infrared

1 Introduction

Over the past few years, near-infrared photodetectors have been widely studied for their great practical importance, such as target detection, telecommunication, and thermal imaging [1–5]. Transition-metal dichalcogenides (TMDCs), a type of two dimensional (2D) materials, have been attracted extensive interest in photodetectors due to their excellent features including ultrathin structure, tunable band structures with different layers, free of dangling bonds and high light absorbance [6–9]. However, most of the photodetectors based on TMDCs such as molybdenum disulfide (MoS_2) and tungsten diselenide (WSe_2) are operated in the visible-wavelength range because of their relative large bandgaps [10–12]. As a new member of TMDCs, molybdenum ditelluride ($MoTe_2$) consists of Te-Mo-Te layers bonded by van der Waals forces. The bandgap of $MoTe_2$ ranges from the indirect bandgap of 0.83 eV for bulk to the direct bandgap of 1.1 eV for monolayer, which is comparably smaller than those of other TMDCs such as MoS_2 and WSe_2 [13]. The small bandgap extends the light absorption spectrum of TMDCs from the visible to the near-infrared, rendering $MoTe_2$ promising for realizing high performance near-infrared photodetectors. The broad spectral range photodetection (0.6–1.55 μm) based on $MoTe_2$ material has been demonstrated [14]. Furthermore, $MoTe_2$-based photodetectors with the structures of metal-semiconductor-metal (MSM) and heterojunction have been intensively investigated [15–18]. For practical photodetectors, fast response speed is particularly important. However, the transit time of carriers between two contact electrodes in the photodetectors based on MSM structure would limit the response speed [19]. As an alternative, photodetectors based on heterojunctions usually rely on the interlayer built-in electric field, which can immediately separate photogenerated electron–hole pairs and result in high speed [20]. In the literatures, many materials have been used to form heterojunction photodetectors with $MoTe_2$, such as MoS_2 [21], graphene [22], and InGaZnO [23]. Germanium (Ge), a semiconductor material of group IV, has the bandgap of 0.67 eV. Owing to its small bandgap induced large absorption coefficient at near-infrared frequencies and excellent compatibility of parallel processing with silicon technology, Ge is also regarded as a good candidate for designing near-infrared photodetectors [24, 25]. Photodetectors based on Ge material with different structures such as MSM, p-i-n, and heterojunction have been widely investigated [26–28]. Furthermore, 2D materials are easily to form heterojunctions with semiconductors. The high performance near-infrared photodetector based on graphene/Ge heterojunction has been demonstrated [29]. However, the combination of $MoTe_2$ and Ge has been not investigated yet, which is desirable to obtain high-performance near-infrared photodetectors.

In this work, we first investigate the $MoTe_2$ and Ge heterojunction for near-infrared photodetector applications. The $MoTe_2$ and Ge heterojunction photodetector shows a high responsivity of 12,460 A/W, a short response time of 5 ms,

---

Address correspondence to Renrong Liang, liangrr@tsinghua.edu.cn; Jun Xu, junxu@tsinghua.edu.cn

and a good specific detectivity of 3.3 × 10^{12} Jones. These results suggest that the $MoTe_2$ and Ge heterojunction shows significant applicability in future high-performance near-infrared photodetectors.

2 Result and discussion

2.1 Characterization of the $MoTe_2$/Ge heterojunction

Bulk 2H-$MoTe_2$ crystals are purchased from HQ Graphene. Figure 1(a) shows the schematic diagram of the $MoTe_2$/Ge heterojunction photodetector. The Ge substrate is intrinsic state without doping. Firstly, a 30-nm-thick Al_2O_3 is deposited on Ge substrate by atomic layer deposition (ALD) at 200 °C and patterned into square matrix with 400 μm × 400 μm using ultra-violet lithography. Then, few-layer $MoTe_2$ materials are produced by the mechanical exfoliation method and transferred to the Ge substrate with patterned Al_2O_3 windows. Before transfer process, the Ge substrate is soaked in 5% HCl solution to remove the surface oxides. And the transfer process is conducted through the poly(dimethylsiloxane) (PDMS)-assisted transfer method, which allows the precise determination of the effective device area located at the window position. Finally, a 40-nm-thick Pt electrode is deposited at the edge of the window area to form the top contact with $MoTe_2$, while a 100-nm-thick Al film serves as the back contact with Ge. The optical image of the as-fabricated device is shown in Fig. 1(b). The $MoTe_2$ film remains continuous and complete after being transferred to the Ge substrate. The atomic force microscopy (AFM) image of the $MoTe_2$/Ge heterojunction is shown in Fig. 1(c). According to the AFM results, the thickness of $MoTe_2$ is approximately 16.2 nm. Figure 1(d) depicts the Raman spectra of the $MoTe_2$/Ge heterojunction, $MoTe_2$ film, and Ge. Three typical Raman peaks and one typical Raman peak are observed on $MoTe_2$ film and Ge, respectively. And these four Raman peaks are both observed on the $MoTe_2$/Ge heterojunction, indicating the interlayer coupling between $MoTe_2$ and Ge. The electrical and optical properties of $MoTe_2$/Ge heterojunction device are characterized with a Keithley 4200-SCS parameter analyzer under a probe station in ambient air at room temperature. The photoresponse is measured under illumination of a laser with the wavelength of 915 nm. And the radius of the laser spot is 0.2 mm, which is large enough to cover the heterojunction. Furthermore, except the $MoTe_2$/Ge heterojunction region, the most area of Ge window is covered with a 100-nm-thick Pt film, which is used to serve as the light blocking layer of the Ge window.

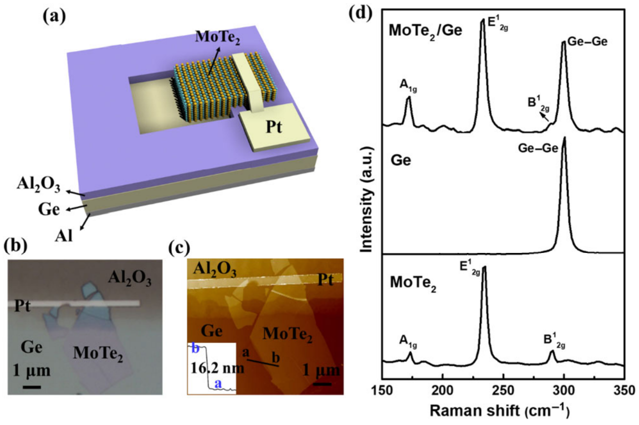

Figure 1 (a) Schematic of the developed $MoTe_2$/Ge heterojunction with patterned window. (b) Optical image of the fabricated $MoTe_2$/Ge heterojunction device. (c) AFM image of the $MoTe_2$/Ge heterojunction. (d) Raman spectra of the $MoTe_2$/Ge heterojunction, Ge and $MoTe_2$.

2.2 Electrical and optical properties of the $MoTe_2$/Ge heterojunction

The current–voltage (I–V) curves of the $MoTe_2$/Ge heterojunction under different light intensities are shown in Fig. 2(a). At dark state, a rectification ratio (the ratio of forward current to reverse current, $|I_{\mathrm{fwd}}|/|I_{\mathrm{rev}}|$) of 133 is obtained. At illuminated states, an obvious photocurrent is observed under reverse bias voltage and the photocurrent increases significantly with the increase of light intensity. However, the photocurrent under forward bias voltage is negligible. The different results between reverse and forward bias voltage arise from that the heterojunction barrier at the $MoTe_2$/Ge interface under reverse bias voltage is larger than that under forward bias voltage and thus a more effective separation of photogenerated electron–hole pairs can be attained under reverse bias voltage. Hence, the photoresponse under reverse bias voltage is much faster than that under forward bias voltage. Moreover, it can also be observed that the minimum current point of the I–V curves shifts toward the forward voltage under illumination. This behavior results from the photovoltaic activity, which indicates that the device can operate without an external power source [30, 31]. Photocurrent (I_{ph}) at $V = -2$ V and $|I_{\mathrm{fwd}}|/|I_{\mathrm{rev}}|$ at $V = \pm 2$ V of the $MoTe_2$/Ge heterojunction are plotted as a function of light intensity as shown in Fig. 2(b). It can be found that I_{ph} at $V = -2$ V is increased almost linearly with the increase of light intensity and the I_{ph} of 44.5 μA is achieved when the power of the incident light is 66.65 mW/cm^2. The exponent θ can be calculated by $I_{\mathrm{ph}} \approx P^{\theta}$ [32–34], where $I_{\mathrm{ph}} = I_{\mathrm{light}} - I_{\mathrm{dark}}$ represents the photocurrent, I_{light} and I_{dark} represent the current at illuminated and dark states, respectively, and P is the light intensity. Through the curve-fitting method with the power function, the θ is estimated to be around 0.93. Furthermore, the $|I_{\mathrm{fwd}}|/|I_{\mathrm{rev}}|$ decreases significantly with the light intensity rising, which results from the significant increase of $|I_{\mathrm{rev}}|$ with light intensity. Photoresponsivity (R) and specific detectivity (D^*) are crucial factors in photodetector performance, which can be calculated by the formula $R = I_{\mathrm{ph}}/PS$ and $D^* = RS^{1/2}/(2qI_{\mathrm{dark}})^{1/2}$, respectively, where S is the effective illumination area and q is the electron charge [33]. Figure 2(c) plots R and D^* of the $MoTe_2$/Ge heterojunction as a function of light intensity at $V = -2$ V. Both R and D^* increase with the increase of light intensity and show relatively high values of 12,460 A/W and 3.3 × 10^{12} Jones when the power of the incident light is 1.09 mW/cm^2, respectively. Moreover, the time-dependent photoresponse properties of the $MoTe_2$/Ge heterojunction are investigated by modulating the laser with a square wave and recording the photocurrent. As shown in Fig. 2(d), the device exhibits good photoswitching stability and high photosensitivity. The rise time (t_{R}) and the decay time (t_{D}) are defined as the time taken to go from 10% to 90% and from 90% to 10% of the total photocurrent, respectively. The regions where current rises and falls with time are enlarged as shown in Figs. 2(e) and 2(f), respectively. Both t_{R} and t_{D} are around 5 ms, indicating that electron–hole pairs are effectively generated, separated, and recombined in the $MoTe_2$/Ge heterojunction.

To better understand the photoresponse mechanism of the $MoTe_2$/Ge heterojunction, the band alignment of the heterojunction is displayed in Fig. 3(a). Since the $MoTe_2$ with Pt contacts is p-type conduction while the Ge is intrinsic state without doping [35, 36], Fermi level of $MoTe_2$ is lower than that of Ge. Therefore, electrons would diffuse from Ge to $MoTe_2$, while holes would diffuse from $MoTe_2$ to Ge. As a result, a built-in electric field is formed at the $MoTe_2$/Ge interface at the equilibrium state as shown in Fig. 3(b). The barrier could

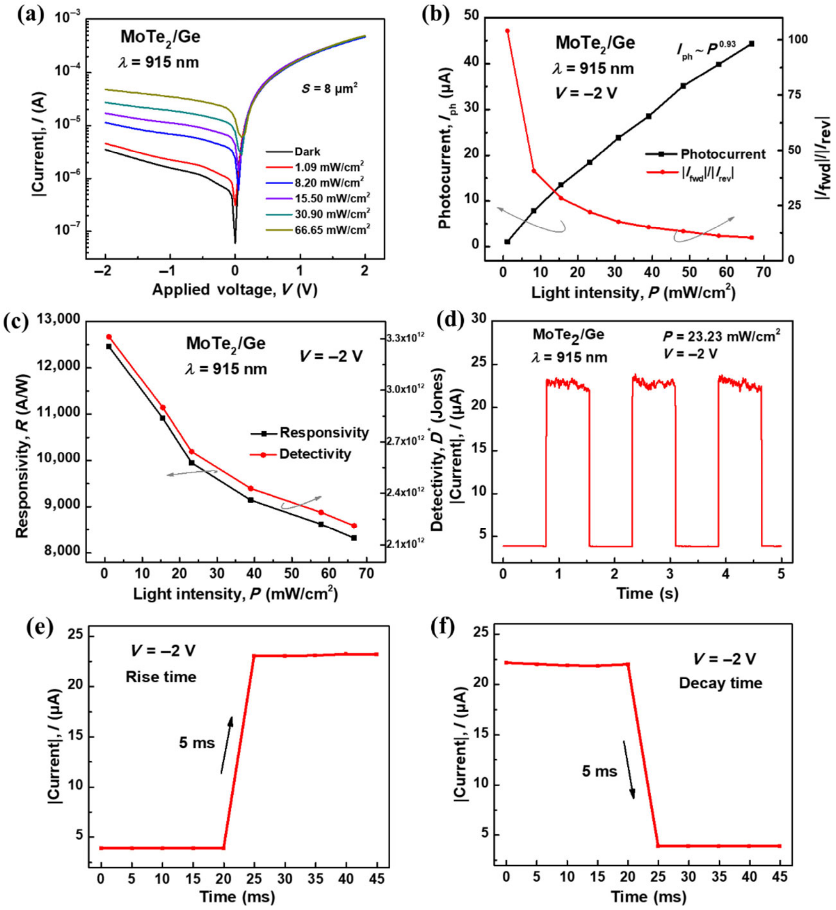

Figure 2 (a) I–V curves of the MoTe$_2$/Ge heterojunction under 915 nm laser illumination with different light intensities. (b) The photocurrents at −2 V and $|I_{\mathrm{fwd}}|/|I_{\mathrm{rev}}|$ at ±2 V of the MoTe$_2$/Ge heterojunction depend on the light intensity. (c) Photoresponsivity and specific detectivity of the MoTe$_2$/Ge heterojunction as a function of light intensity. (d) The continuous current–time cycles of the MoTe$_2$/Ge heterojunction. The enlarged regions where current (e) rises and (f) falls with time.

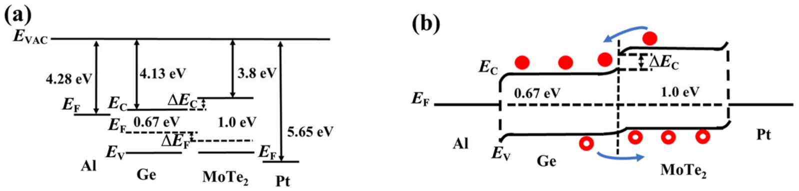

Figure 3 (a) Band alignments of the MoTe$_2$/Ge heterojunction. (b) Energy band diagrams of the MoTe$_2$/Ge heterojunction at the equilibrium state.

be adjusted by the bias voltage, which will be increased under reverse bias voltage while decreased under forward bias voltage. Furthermore, the Schottky barriers between semiconductors (MoTe$_2$ and Ge) and contact metals (Al and Pt) are formed [35, 36]. When the photodetector is under illumination, Ge and MoTe$_2$ both absorb photons to generate electron–hole pairs, then the photoexcited electron–hole pairs will be separated by the built-in electric field at the MoTe$_2$/Ge interface and the Schottky barriers between semiconductors (MoTe$_2$ and Ge) and contact metals (Al and Pt). And this process leads to the generation of photocurrent in the device.

2.3 Electrical and optical properties of the MoTe$_2$/GeO$_2$/Ge heterojunction

As shown in Fig. 3(a), the ΔE_c between MoTe$_2$ and Ge is 0.33 eV And the ΔE_v between MoTe$_2$ and Ge is almost negligible. Hence, the hot carriers generated and transported between MoTe$_2$ and Ge are large, leading to a non-negligible reverse current at dark (I_{leak}). The I_{leak} of the MoTe$_2$/Ge heterojunction is 0.44 μA/μm^2. The large I_{leak} may limit the further performance improvements and increase the power consumption of the photodetectors. It has been reported that inserting an interfacial oxide layer would reduce the I_{leak} in the graphene/Si heterojunction photodetector [37]. Therefore, in order to effectively suppress the I_{leak} of the MoTe$_2$/Ge heterojunction, an ultrathin interfacial GeO$_2$ layer is inserted between MoTe$_2$ and Ge in this work. Before the transfer of the MoTe$_2$ film, the GeO$_2$ layer is grown on the patterned Ge substrate by ozone oxidation at 300 °C for 30 min using the same ALD system. The schematic diagram is shown in Fig. 4(a), where a GeO$_2$ layer is sandwiched between MoTe$_2$ and Ge. The band diagram of the MoTe$_2$/GeO$_2$/Ge heterojunction is shown in Fig. 4(b). The thin GeO$_2$ layer serves as a blocking layer to reduce hot carriers transporting between MoTe$_2$ and Ge and thus suppress the I_{leak} of the MoTe$_2$/Ge heterojunction. The MoTe$_2$/GeO$_2$/Ge heterojunction is characterized by transmission electron microscope (TEM) as shown in Fig. 4(c). A 2-nm-thick GeO$_2$ layer is formed on the surface of Ge after ozone oxidation. And the MoTe$_2$ is around 21 layers with the thickness of around 16 nm, which is similar with that of the MoTe$_2$/Ge heterojunction. The I–V curves under dark of the MoTe$_2$/Ge heterojunction with and without

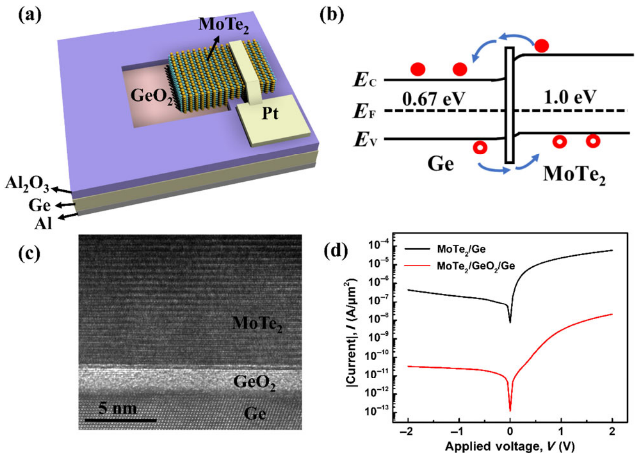

Figure 4 (a) The schematic diagram of the MoTe$_2$/GeO$_2$/Ge heterojunction. (b) Energy band diagrams of the MoTe$_2$/GeO$_2$/Ge heterojunction at the equilibrium state. (b) The TEM image of the MoTe$_2$/GeO$_2$/Ge heterojunction. (d) The *I*–*V* curves under dark of the MoTe$_2$/Ge heterojunction with and without GeO$_2$ layer.

GeO$_2$ layer are plotted in Fig. 4(d). After the insertion of GeO$_2$ layer, the I_{leak} is reduced by more than four orders of magnitude, reaching to a very small value of 0.03 nA/μm^2. Furthermore, the forward current at dark is also reduced due to the existence of the GeO$_2$ layer, which results from that the GeO$_2$ layer would also block the transport of carriers under forward bias voltage. However, the reduction under reverse current is more obvious than that under forward current, leading to the increase of the rectification ratio after inserting the GeO$_2$ layer. A rectification ratio of 654 is obtained after the insertion of the GeO$_2$ layer, compared to that of 133 without the GeO$_2$ layer.

After optimizing the I_{leak} of the MoTe$_2$/Ge heterojunction by inserting a GeO$_2$ layer, the optoelectronic properties of the MoTe$_2$/GeO$_2$/Ge heterojunction are systematically investigated. The *I*–*V* characteristics of the MoTe$_2$/GeO$_2$/Ge heterojunction under 915 nm laser illumination at different light intensities are shown in Fig. 5(a). Consistent with the MoTe$_2$/Ge heterojunction without the GeO$_2$ layer, an obvious photocurrent can be observed under reverse bias voltage while negligible photocurrent is attained under forward bias voltage at illuminated states. The current increases significantly under reverse bias voltages as the light intensity increases. Furthermore, the minimum current point of the *I*–*V* curve also shifts toward the forward voltage under illumination, which is like the results of the MoTe$_2$/Ge heterojunction without the GeO$_2$ layer. And the shift is more obvious in the MoTe$_2$/GeO$_2$/Ge heterojunction, which indicates that the photovoltaic activity is more obvious after the insertion of the GeO$_2$ layer. Figure 5(b) shows the I_{ph} at −2 V and $|I_{\text{fwd}}|/|I_{\text{rev}}|$ at ±2 V as a function of light intensity for the MoTe$_2$/GeO$_2$/Ge heterojunction. The I_{ph} increases and the $|I_{\text{fwd}}|/|I_{\text{rev}}|$ decreases significantly with the light intensity rising. And the θ of I_{ph} and light intensity is estimated to be around 1. When the power of the incident light is 66.65 mW/cm^2, the I_{ph} of 0.73 μA is achieved. The value is smaller than that of the MoTe$_2$/Ge heterojunction without the GeO$_2$ layer, which results from the existence of the GeO$_2$ block layer. *R* and D^* of the MoTe$_2$/GeO$_2$/Ge heterojunction as a function of light intensity

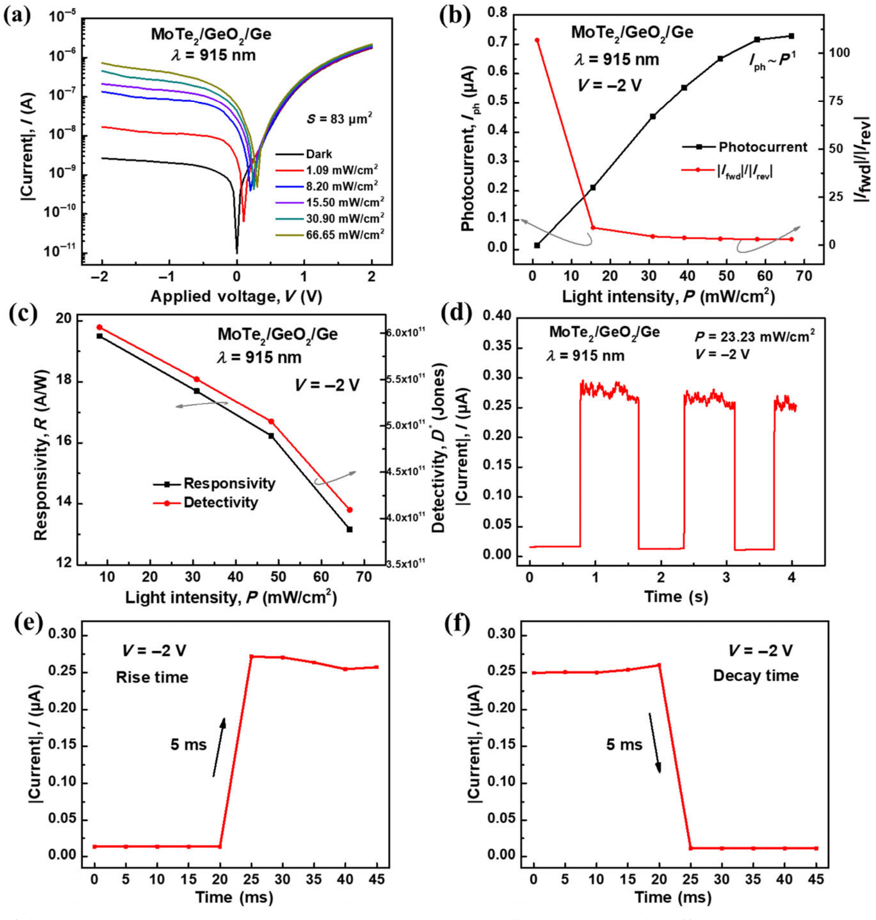

Figure 5 (a) *I*–*V* curves of the MoTe$_2$/GeO$_2$/Ge heterojunction under 915 nm laser illumination with different light intensities. (b) The photocurrents at −2 V and $|I_{\text{fwd}}|/|I_{\text{rev}}|$ at ±2 V of the MoTe$_2$/GeO$_2$/Ge heterojunction depend on the light intensity. (c) Photoresponsivity and specific detectivity of the MoTe$_2$/GeO$_2$/Ge heterojunction as a function of light intensity. (d) The continuous current–time cycles of the MoTe$_2$/GeO$_2$/Ge heterojunction. The enlarged regions where current (e) rises and (f) falls with time.

at −2 V are displayed in Fig. 5(c). The maximum values of R and D^* are 15.6 A/W and 4.86 × 10^{11} Jones, respectively when the power of the incident light is 1.09 mW/cm^2. The reduced R and D^* in the $MoTe_2/GeO_2/Ge$ heterojunction result from the reduced I_{ph}. However, they are still compared to those of other reported $MoTe_2$-based photodetectors [14, 35, 38, 39]. The time-dependent photoresponse properties of the $MoTe_2/GeO_2/Ge$ heterojunction are also investigated. As shown in Fig. 5(d), the good photoswitching stability is well-preserved after the insertion of the GeO_2 layer. The regions where current rises and falls with time are enlarged as shown in Figs. 5(e) and 5(f), respectively. Both t_R and t_D are 5 ms, which is consistent with the $MoTe_2/Ge$ heterojunction without the GeO_2 layer. It indicates that the effect of the generation, separation and recombination of electron–hole pairs are still effective in the $MoTe_2/Ge$ heterojunction after inserting the GeO_2 layer. Table 1 presents the characteristic comparison of the $MoTe_2/Ge$ heterojunction with/without a GeO_2 layer with other $MoTe_2$-based photodetectors in previous reports. The heterostructures in this work display good comprehensive photodetection performance, which indicates the $MoTe_2/Ge$ heterostructure has great potential in applications for future photodetectors.

Table 1 Performance comparison of the photodetectors in this work with other reported $MoTe_2$-based photodetectors

Materials	Wavelength (nm)	Responsivity (A/W)	Response time (ms)	Detectivity (Jones)	Ref.
$MoTe_2/Ge$	915	12,460	5	3.3 × 10^{12}	This work
$MoTe_2/GeO_2/Ge$	915	15.6	5	4.86 × 10^{11}	This work
$MoTe_2$	1,060	0.024	1.3	1.3 × 10^9	[14]
$MoTe_2$	680	6	0.16	—	[35]
$MoTe_2$/graphene	1,064	970	78	1.55 × 10^{11}	[38]
$MoTe_2/MoS_2$	633	0.073	68	—	[39]

3 Conclusions

In summary, a high-performance near-infrared photodetector is obtained based on the structure of $MoTe_2/Ge$ heterojunction. The optoelectronic properties of the $MoTe_2/Ge$ heterojunction under 915 nm laser illumination have been systematically studied. The $MoTe_2/Ge$ heterojunction photodetector shows good optoelectronic performances with photoresponsivity and specific detectivity of as high as 12,460 A/W and 3.3 × 10^{12} Jones, respectively. And the photoresponse time of 5 ms is attained. Moreover, in order to reduce the reverse current at dark, a thin GeO_2 layer is introduced to the $MoTe_2/Ge$ heterojunction. After inserting the GeO_2 layer, the reverse current at dark of the $MoTe_2/Ge$ heterojunction is reduced by more than four orders of magnitude. And the $MoTe_2/Ge$ heterojunction with a GeO_2 layer also exhibits good optoelectronic performances with high responsivity (15.6 A/W), short response time (5 ms), and good specific detectivity (4.86 × 10^{11} Jones), which is compared to those of other reported $MoTe_2$-based photodetectors. All these results make $MoTe_2/Ge$ heterojunction a promising structure for next generation high-performance photodetectors.

Acknowledgements

This work was supported by the National Key Research and Development Program of China (Nos. 2016YFA0200400 and 2016YFA0302300) and the National Science and Technology Major Project of China (No. 2016ZX02301001).

References

[1] Gobin, A. M.; Lee, M. H.; Halas, N. J.; James, W. D.; Drezek, R. A.; West, J. L. Near-infrared resonant nanoshells for combined optical imaging and photothermal cancer therapy. *Nano Lett.* **2007**, *7*, 1929–1934.

[2] Miao, J. S.; Hu, W. D.; Guo, N.; Lu, Z. Y.; Liu, X. Q.; Liao, L.; Chen, P. P.; Jiang, T.; Wu, S. W.; Ho, J. C. et al. High-responsivity graphene/InAs nanowire heterojunction near-infrared photodetectors with distinct photocurrent on/off ratios. *Small* **2015**, *11*, 936–942.

[3] Luo, L. B.; Chen, J. J.; Wang, M. Z.; Hu, H.; Wu, C. Y.; Li, Q.; Wang, L.; Huang, J. A.; Liang, F. X. Near-infrared light photovoltaic detector based on GaAs nanocone array/monolayer graphene schottky junction. *Adv. Funct. Mater.* **2014**, *24*, 2794–2800.

[4] Zhu, S. Y.; Yu, M. B.; Lo, G. Q.; Kwong, D. L. Near-infrared waveguide-based nickel silicide Schottky-barrier photodetector for optical communications. *Appl. Phys. Lett.* **2008**, *92*, 081103.

[5] Geis, M. W.; Spector, S. J.; Grein, M. E.; Schulein, R. T.; Yoon, J. U.; Lennon, D. M.; Deneault, S.; Gan, F.; Kaertner, F. X.; Lyszczarz, T. M. CMOS-compatible all-Si high-speed waveguide photodiodes with high responsivity in near-infrared communication band. *IEEE Photonics Technol. Lett.* **2007**, *19*, 152–154.

[6] Wang, X. D.; Wang, P.; Wang, J. L.; Hu, W. D.; Zhou, X. H.; Guo, N.; Huang, H.; Sun, S.; Shen, H.; Lin, T. et al. Ultrasensitive and broadband MoS_2 photodetector driven by ferroelectrics. *Adv. Mater.* **2015**, *27*, 6575–6581.

[7] Ye, L.; Li, H.; Chen, Z. F.; Xu, J. B. Near-infrared photodetector based on MoS_2/black phosphorus heterojunction. *Acs Photonics* **2016**, *3*, 692–699.

[8] Ye, L.; Wang, P.; Luo, W. J.; Gong, F.; Liao, L.; Liu, T. D.; Tong, L.; Zang, J. F.; Xu, J. B.; Hu, W. D. Highly polarization sensitive infrared photodetector based on black phosphorus-on-WSe_2 photogate vertical heterostructure. *Nano Energy* **2017**, *37*, 53–60.

[9] Kang, D. H.; Kim, M. S.; Shim, J.; Jeon, J.; Park, H. Y.; Jung, W. S.; Yu, H. Y.; Pang, C. H.; Lee, S.; Park, J. H. High-performance transition metal dichalcogenide photodetectors enhanced by self-assembled monolayer doping. *Adv. Funct. Mater.* **2015**, *25*, 4219–4227.

[10] De Fazio, D.; Goykhman, I.; Yoon, D.; Bruna, M.; Eiden, A.; Milana, S.; Sassi, U.; Barbone, M.; Dumcenco, D.; Marinov, K. et al. High responsivity, large-area graphene/MoS_2 flexible photodetectors. *ACS Nano* **2016**, *10*, 8252–8262.

[11] Zhang, W. J.; Chiu, M. H.; Chen, C. H.; Chen, W.; Li, L. J.; Wee, A. T. S. Role of metal contacts in high-performance phototransistors based on WSe_2 monolayers. *ACS Nano* **2014**, *8*, 8653–8661.

[12] Yu, S. H.; Lee, Y.; Jang, S. K.; Kang, J.; Jeon, J.; Lee, C.; Lee, J. Y.; Kim, H.; Hwang, E.; Lee, S. et al. Dye-sensitized MoS_2 photodetector with enhanced spectral photoresponse. *ACS Nano* **2014**, *8*, 8285–8291.

[13] Keum, D. H.; Cho, S.; Kim, J. H.; Choe, D. H.; Sung, H. J.; Kan, M.; Kang, H.; Hwang, J. Y.; Kim, S. W.; Yang, H. et al. Bandgap opening in few-layered monoclinic $MoTe_2$. *Nat. Phys.* **2015**, *11*, 482–486.

[14] Huang, H.; Wang, J. L.; Hu, W. D.; Liao, L.; Wang, P.; Wang, X. D.; Gong, F.; Chen, Y.; Wu, G. J.; Luo, W. J. et al. Highly sensitive visible to infrared $MoTe_2$ photodetectors enhanced by the photogating effect. *Nanotechnology* **2016**, *27*, 445201.

[15] Yin, L.; Zhan, X. Y.; Xu, K.; Wang, F.; Wang, Z. X.; Huang, Y.; Wang, Q. S.; Jiang, C.; He, J. Ultrahigh sensitive $MoTe_2$ phototransistors driven by carrier tunneling. *Appl. Phys. Lett.* **2016**, *108*, 043503.

[16] Huang, H.; Wang, X. D.; Wang, P.; Wua, G. J.; Chen, Y.; Meng, C. M.; Liao, L.; Wang, J. L.; Hu, W. D.; Shen, H. et al. Ferroelectric polymer tuned two dimensional layered $MoTe_2$ photodetector. *RSC Adv.* **2016**, *6*, 87416–87421.

[17] Zhang, K. A.; Zhang, T. N.; Cheng, G. H.; Li, T. X.; Wang, S. X.; Wei, W.; Zhou, X. H.; Yu, W. W.; Sun, Y.; Wang, P. et al. Interlayer transition and infrared photodetection in atomically thin type-II $MoTe_2/MoS_2$ van der Waals heterostructures. *ACS Nano* **2016**, *10*, 3852–3858.

[18] Kuiri, M.; Chakraborty, B.; Paul, A.; Das, S.; Sood, A. K.; Das, A. Enhancing photoresponsivity using $MoTe_2$-graphene vertical heterostructures. *Appl. Phys. Lett.* **2016**, *108*, 063506.

[19] Xie, C.; Mak, C.; Tao, X. M.; Yan, F. Photodetectors based on two-dimensional layered materials beyond graphene. *Adv. Funct. Mater.* **2017**, *27*, 1603886.

[20] Wang, J. L.; Fang, H. H.; Wang, X. D.; Chen, X. S.; Lu, W.; Hu, W. D. Recent progress on localized field enhanced two-dimensional material photodetectors from ultraviolet–visible to infrared. *Small* **2017**, *13*, 1700894.

[21] Pezeshki, A.; Shokouh, S. H. H.; Nazari, T.; Oh, K.; Im, S. electric and photovoltaic behavior of a few-layer α-$MoTe_2$/MoS_2 dichalcogenide heterojunction. *Adv. Mater.* **2016**, *28*, 3216–3222.

[22] Zhang, K.; Fang, X.; Wang, Y. L.; Wan, Y.; Song, Q. J.; Zhai, W. H.; Li, Y. P.; Ran, G. Z.; Ye, Y.; Dai, L. Ultrasensitive near-infrared photodetectors based on a graphene–$MoTe_2$–graphene vertical van der Waals heterostructure. *ACS Appl. Mater. Interfaces* **2017**, *9*, 5392–5398.

[23] Lee, H. S.; Choi, K.; Kim, J. S.; Yu, S.; Ko, K. R.; Im, S. Coupling two-dimensional $MoTe_2$ and InGaZnO thin-film materials for hybrid PN junction and CMOS inverters. *ACS Appl. Mater. Interfaces* **2017**, *9*, 15592–15598.

[24] Colace, L.; Masini, G.; Assanto, G.; Luan, H. C.; Wada, K.; Kimerling, L. C. Efficient high-speed near-infrared Ge photodetectors integrated on Si substrates. *Appl. Phys. Lett.* **2000**, *76*, 1231–1233.

[25] Masini, G.; Calace, L.; Assanto, G.; Luan, H. C.; Kimerling, L. C. High-performance p-i-n Ge on Si photodetectors for the near infrared: From model to demonstration. *IEEE Trans. Electron Dev.* **2001**, *48*, 1092–1096.

[26] Ang, K. W.; Zhu, S. Y.; Wang, J.; Chua, K. T.; Yu, M. B.; Lo, G. Q.; Kwong, D. L. Novel silicon-carbon (Si:C) schottky barrier enhancement layer for dark-current suppression in Ge-on-SOI MSM photodetectors. *IEEE Electron Device Lett.* **2008**, *29*, 704–707.

[27] Virot, L.; Benedikovic, D.; Szelag, B.; Alonso-Ramos, C.; Karakus, B.; Hartmann, J. M.; Le Roux, X.; Crozat, P.; Cassan, E.; Marris-Morini, D. et al. Integrated waveguide PIN photodiodes exploiting lateral Si/Ge/Si heterojunction. *Opt. Express* **2017**, *25*, 19487–19496.

[28] Tseng, C. K.; Chen, W. T.; Chen, K. H.; Liu, H. D.; Kang, Y. M.; Na, N. L.; Lee, M. C. M. A self-assembled microbonded germanium/silicon heterojunction photodiode for 25 Gb/s high-speed optical interconnects. *Sci. Rep.* **2013**, *3*, 3225.

[29] Zeng, L. H.; Wang, M. Z.; Hu, H.; Nie, B.; Yu, Y. Q.; Wu, C. Y.; Wang, L.; Hu, J. G.; Xie, C.; Liang, F. X. et al. Monolayer graphene/germanium schottky junction as high-performance self-driven infrared light photodetector. *ACS Appl. Mater. Interfaces* **2013**, *5*, 9362–9366.

[30] Gao, Z. W.; Jin, W. F.; Zhou, Y.; Dai, Y.; Yu, B.; Liu, C.; Xu, W. J.; Li, Y. P.; Peng, H. L.; Liu, Z. F. et al. Self-powered flexible and transparent photovoltaic detectors based on CdSe nanobelt/graphene Schottky junctions. *Nanoscale* **2013**, *5*, 5576–5581.

[31] Park, S.; Heo, S. W.; Lee, W.; Inoue, D.; Jiang, Z.; Yu, K.; Jinno, H.; Hashizume, D.; Sekino, M.; Yokota, T. et al. Self-powered ultra-flexible electronics via nano-grating-patterned organic photovoltaics. *Nature* **2018**, *561*, 516–521.

[32] Wu, E. P.; Wu, D.; Jia, C.; Wang, Y. G.; Yuan, H. Y.; Zeng, L. H.; Xu, T. T.; Shi, Z. F.; Tian, Y. T.; Li, X. J. *In situ* fabrication of 2D WS_2/Si type-II heterojunction for self-powered broadband photodetector with response up to mid-infrared. *ACS Photonics* **2019**, *6*, 565–572.

[33] Xiao, P.; Mao, J.; Ding, K.; Luo, W. J.; Hu, W. D.; Zhang, X. J.; Zhang, X. H.; Jie, J. S. Solution-processed 3D RGO–MoS_2/pyramid Si heterojunction for ultrahigh detectivity and ultra-broadband photodetection. *Adv. Mater.* **2018**, *30*, 1801729.

[34] Wu, D.; Guo, J. W.; Du, J.; Xia, C. X.; Zeng, L. H.; Tian, Y. Z.; Shi, Z. F.; Tian, Y. T.; Li, X. J.; Tsang, Y. H. et al. Highly polarization-sensitive, broadband, self-powered photodetector based on graphene/$PdSe_2$/germanium heterojunction. *ACS Nano* **2019**, *13*, 9907–9917.

[35] Octon, T. J.; Nagareddy, V. K.; Russo, S.; Craciun, M. F.; Wright, C. D. Fast high-responsivity few-layer $MoTe_2$ photodetectors. *Adv. Opt. Mater.* **2016**, *4*, 1750–1754.

[36] Sun, C. C.; Liang, R. R.; Liu, L. B.; Wang, J.; Xu, J. Leakage current of germanium-on-insulator-based junctionless nanowire transistors. *Appl. Phys. Lett.* **2015**, *107*, 132105.

[37] Li, X. M.; Zhu, M.; Du, M. D.; Lv, Z.; Zhang, L.; Li, Y. C.; Yang, Y.; Yang, T. T.; Li, X.; Wang, K. L. et al. High detectivity graphene-silicon heterojunction photodetector. *Small* **2016**, *12*, 595–601.

[38] Yu, W. Z.; Li, S. J.; Zhang, Y. P.; Ma, W. L.; Sun, T.; Yuan, J.; Fu, K.; Bao, Q. L. Near-infrared photodetectors based on $MoTe_2$/graphene heterostructure with high responsivity and flexibility. *Small* **2017**, *13*, 1700268.

[39] Wang, B.; Yang, S. X.; Wang, C.; Wu, M. H.; Huang, L.; Liu, Q.; Jiang, C. B. Enhanced current rectification and self-powered photoresponse in multilayer p-$MoTe_2$/n-MoS_2 van der Waals heterojunctions. *Nanoscale* **2017**, *9*, 10733–10740.